



Roberto C. Gallo-Villanueva^{1*}
 Victor H. Perez-Gonzalez^{1*}
 Braulio Cardenas-Benitez^{1*}
 Binny Jind¹
 Sergio O. Martinez-Chapa¹
 Blanca H. Lapizco-Encinas²

¹School of Engineering and Sciences, Nano- Sensors and Devices Research Group, Tecnológico de Monterrey, Monterrey, NL, Mexico

²Microscale Bioseparations Laboratory, Rochester Institute of Technology, Rochester, NY, USA

Received November 21, 2018

Revised March 8, 2019

Accepted March 8, 2019

Research Article

Joule heating effects in optimized insulator-based dielectrophoretic devices: An interplay between post geometry and temperature rise

Insulator-based dielectrophoresis (iDEP) is the electrokinetic migration of polarized particles when subjected to a non-uniform electric field generated by the inclusion of insulating structures between two remote electrodes. Electrode spacing is considerable in iDEP systems when compared to electrode-based DEP systems, therefore, iDEP systems require high voltages to achieve efficient particle manipulation. A consequence of this is the temperature increase within the channel due to Joule heating effects, which, in some cases, can be detrimental when manipulating biological samples. This work presents an experimental and modeling study on the increase in temperature inside iDEP devices. For this, we studied seven distinct channel designs that mainly differ from each other in their post array characteristics: post shape, post size and spacing between posts. Experimental results obtained using a custom-built copper Resistance Temperature Detector, based on resistance changes, show that the influence of the insulators produces a difference in temperature rise of approximately 4°C between the designs studied. Furthermore, a 3D COMSOL model is also introduced to evaluate heat generation and dissipation, which is in good agreement with the experiments. The model allowed relating the difference in average temperature for the geometries under study to the electric resistance posed by the post array in each design.

Keywords:

Dielectrophoresis / Joule heating / Microfluidics / Sensors / Temperature

DOI 10.1002/elps.201800490



Additional supporting information may be found online in the Supporting Information section at the end of the article.

1 Introduction

Owing to its potential to replace laboratory equipment for many bioanalytical applications with small, inexpensive, portable, and easy-to-use devices, microfluidics has emerged as a critical research field [1]. Microfluidic technology allows manipulating fluid samples using thermal, acoustic, mechanical, or electromagnetic phenomena [2]. One fundamental sample processing step, common to all bioanalytical applications, is particle actuation (i.e., filtration, isolation,

concentration, separation, or transportation) for which electric-field-driven microfluidic methods have been proven to be effective [3].

Dielectrophoresis (DEP) refers to the force acting on polarizable particles when subjected to a spatially non-uniform electric field [4]. In insulator-based dielectrophoresis (iDEP), an electric field is commonly generated between electrodes placed at the inlet and outlet of the microfluidic device. This field is distorted by the presence of a set of insulating structures fabricated within the microchannel, rendering significant spatial non-uniformities in its distribution [5]. Insulator-based DEP devices offer many attractive traits (e.g., low cost, low fabrication complexity, and material transparency) [6] and therefore have been used to manipulate many types of bioparticles [7–12]. Nonetheless, due to the electric charges present in the channel and particles surfaces, and to ions in solution,

Correspondence: Dr. Blanca H. Lapizco-Encinas, Microscale Bioseparations Laboratory, Biomedical Engineering Department, Rochester Institute of Technology, Rochester NY 14623, USA
Fax: +1-585-475-5041
E-mail: bhlbme@rit.edu

Abbreviations: DEP, dielectrophoresis; iDEP, insulator-based dielectrophoresis; PCB, printed circuit board; PSA, pressure sensitive adhesive; RTD, resistance temperature detector

*These authors contributed equally to this work.

Color online: See the article online to view Figs. 1–5 in color.

electrophoresis (EP) and electroosmosis (EO) compete with DEP in controlling particle motion [13]. This, in addition to the long distance between electrodes in iDEP-based devices ($\sim 10^{-2}$ m), significantly increases the stimulation voltage requirements for the device, reaching values in the 10^2 – 10^3 V range [14].

Joule heating is an electrothermal effect that takes place in conductive media subjected to electric stimulation [15]. iDEP is particularly susceptible to Joule heating as most biological particles must be suspended in highly conductive solutions to preserve their function [16]. Temperature rise poses a risk to biological particles; e.g., it was reported that heating a sample of *Mycobacterium tuberculosis* at temperatures above 56°C produces cell death [17]. It is also known that a wide range of proteins undergo heat denaturation at temperatures higher than 80°C [18]. Moreover, Joule heating presents another side-effect, i.e., electrothermal flow, which can affect particle trapping efficiency in iDEP systems [19]. Temperature control strategies are thus needed to reduce adverse experimental effects in microfluidics [20]. In addition, predicting and monitoring temperature rise due to Joule heating in microfluidic devices is of utmost importance.

Computational models have been used extensively to study thermal effects in microfluidic systems. In 2010, Hawkins et al. analyzed electrothermally-induced flow in iDEP systems [21]. In their work, DC-biased AC fields were used as electric stimulation. Predictions indicated that for most scenarios tested, electrothermal flow enhanced negative DEP trapping. Although their findings are related to electrically-induced thermal effects, their focus is on flow fields and not on temperature measurement. Later, in 2011, Sridharan et al. used a computational model to predict the effects of Joule heating in electroosmotic flow [22]. This work presented the first experimental approach to study such effect in a typical iDEP device under DC-biased AC voltages. The model was validated with experimental flow field measurements. They concluded that observed fluid circulations were due to Joule heating induced flow inhomogeneities in the constriction region of the channel interacting with the electric field. Since then, many reports have become available in the literature where computational models predict electrothermal effects and are validated through flow field experimental observations [12, 16, 23–27]. These studies made the dependence of Joule heating on the electric field spatial distribution (and therefore on channel geometry) evident. However, no experimental temperature measurements were presented to validate such dependency.

In 2001, Ross et al. developed an experimental protocol to monitor temperature rise in microfluidic systems using Rhodamine B, a temperature-dependent fluorescent dye [28]. Nakano et al. employed a similar method to resolve spatial and temporal measurements of temperature rise in iDEP devices [29]. In their work, Nakano et al. took two different routes to measure temperature. In the first approach, the temperature sensitive Rhodamine B was mixed with a surfactant and loaded into the microfluidic devices, and heating was directly monitored during voltage application. The second approach

included the use of a thin PDMS film doped with Rhodamine B located at the bottom of the device, serving as an indirect temperature sensitive element. Both approaches resulted in experimental observations that were in good agreement with predictions obtained from a computational model. However, temperature sensitive dyes are known to be prone to photobleaching, both through exposure to the incoming light and by large temperature fluctuations, leading to changes in the baseline fluorescence intensity [28]. In addition, optical detection might not be amenable to miniaturization and data acquisition. Nonetheless, to the best of our knowledge, the report by Nakano et al. is the only currently available experimental protocol for temporal and spatial temperature monitoring in iDEP devices.

The present contribution studies Joule heating effects on a range of iDEP devices. Such devices were selected from a previous report by our group [30], in which we predicted the most effective post array characteristics: post shape, post size and spacing between posts to maximize particle trapping in iDEP devices by negative DEP [30]. Herein, we analyze the performance of seven distinct iDEP channel designs in terms of Joule heating. We performed extensive numerical modeling with COMSOL Multiphysics®, which was validated by experimentation. A copper Resistance Temperature Detector (RTD) sensor was employed for experimentally assessing the overall temperature of the device. Our results demonstrated that the overall temperature rise in the devices is small (in good agreement with other reports [29]) and that differences in temperature rise among the distinct iDEP designs studied were also small. These results are encouraging since optimized designs can achieve significant particle trapping at much lower voltages than traditional iDEP devices.

2 Theory and computational model

The dielectrophoretic force, F_{DEP} , exerted on a polarizable spherical particle suspended in solution is given by the expression:

$$\mathbf{F}_{DEP} = 2\pi a^3 \epsilon_m \text{Re}\{K\} \nabla(\mathbf{E} \cdot \mathbf{E}) \quad (1)$$

where a is the microsphere radius, ϵ_m is the permittivity of the suspending solution, \mathbf{E} is the electric field intensity vector, and K is the complex Clausius-Mossotti factor, defined as:

$$K = \frac{\epsilon_p^* - \epsilon_m^*}{\epsilon_p^* + 2\epsilon_m^*} \quad (2)$$

with $\epsilon_i^* = \epsilon_i - j\sigma_i/\omega$ being the complex permittivity and where $j = \sqrt{-1}$. The complex permittivity is a function of the electric stimulation angular frequency (ω), and of the permittivity (ϵ) and conductivity (σ) of the material ($i = p$ for particle, $i = m$ for suspending solution). However, because our experimental setup involved only direct current (DC) electric stimulation (i.e., $\omega = 0$), Eq. (2) can be simplified to:

$$K = \frac{\sigma_p - \sigma_m}{\sigma_p + 2\sigma_m} \quad (3)$$

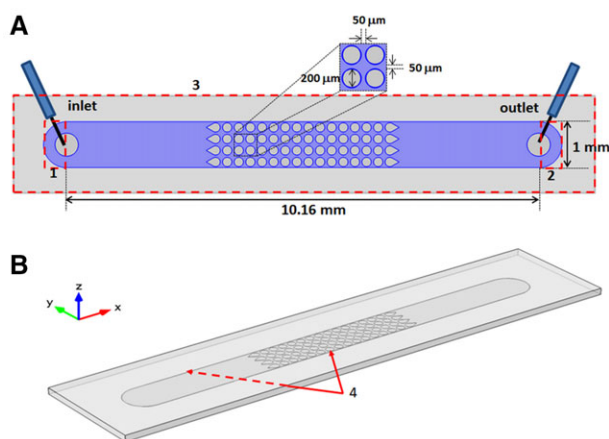


Figure 1. (A) Schematic representation of the top view, and (B) 3D representation of one of the microchannel designs (original circles) used in this study indicating the domains and boundaries employed in the COMSOL model, which are defined in Supporting Information Table 1. The specific dimensions for all six designs employed in this study are listed in Table 1.

For further details on the simplification of Eq. (3), the reader is referred to ref. 31, 32. The CM factor given by Eq. (3) is no longer a complex number and the values it can take are limited between -0.5 and 1 . By definition, \mathbf{F}_{DEP} always points in the direction of the field gradient $\nabla(\mathbf{E} \cdot \mathbf{E})$ for $K > 0$. This is known as positive DEP and particles are attracted to the regions of high field gradient. Conversely, for $K < 0$ the force direction is reversed in Eq. (1), giving rise to negative DEP where particles are repelled from high field gradient zones.

Joule heating effects are important in all electric-field driven applications, such as dielectrophoretic devices. When an electric current flows through an ionic fluid, temperature rises by increasing the applied voltage and/or the fluid conductivity. When analyzing this, the fluid flow velocity (\mathbf{v}_{fluid}) must be considered. In the absence of pressure gradients, the only mechanism in the system that creates fluid motion is electroosmosis. Therefore, in our model:

$$\mathbf{v}_{fluid} = \mathbf{v}_{EK} = - \left(\frac{\epsilon_m \zeta_{PDMS}}{\eta_m} \right) \mathbf{E} \quad (4)$$

where ζ_{PDMS} is the zeta potential of the PDMS walls and η_m is the viscosity of the suspending medium.

The spatial distribution of the electric potential, ϕ , was obtained by solving the Laplace equation using the Electric Currents Module in COMSOL Multiphysics v5.3a (COMSOL Inc., Burlington, MA, USA). From this, the electric field is calculated as $\mathbf{E} = -\nabla\phi$. Moreover, the temperature distribution across the different microfluidic channels used in this work was estimated by coupling the Electric Currents Module to the Heat Transfer and Multiphysics Modules in COMSOL. Figure 1 illustrates one of the channel designs employed in this study, and Table 1 lists the dimensions for all channel designs. The domains and boundary conditions used in our model to analyze the interrelation between the electric field

(needed to drive the dielectrophoretic effect), the fluid flow, and heat transfer phenomena are indicated in Fig. 1 and Supporting Information Table 1, respectively. Supporting Information Table 2 lists the model and mesh parameters employed in the COMSOL Multiphysics model. It is important to note that materials properties (e.g., electrical conductivity, thermal conductivity, viscosity, etc.) are temperature dependent functions. The computational model takes this into consideration and calculates the changes of such properties over the time course of the simulated experiment.

3 Materials and methods

3.1 Microdevices

Joule heating effects were evaluated in seven different microchannel designs fabricated with PDMS using soft-lithography procedures as described in a recent contribution from our group [33]. Briefly, to create a master, SU-8 2007 (MicroChem, USA) was spun into a 5×5 cm glass slide using a spin coater model WS-650 HZB-23NPP/UD3 (Laurell Technologies Corporation, USA), following the supplier recommendations to obtain a $7 \mu\text{m}$ thick layer. The photoresist was then exposed to UV light through masks with the desired designs, and un-exposed material was removed using a developer to create masters. Degassed PDMS (Sylgard 184, Dow Corning, USA) mixed in a 10:1 ratio of monomers with the curing agent was poured on top of the master and heated to 120°C on a hot plate for 15 min. Solidified PDMS was removed from the masters and holes were punched using a 1 mm core bore to create reservoirs.

The channel designs evaluated in this study were developed based on a numerical and parametric optimization process that started with the two most common geometries (referred to as original designs) used in iDEP devices, i.e., circular-shaped posts and diamond-shaped posts. The optimization process led to sub-optimized geometries, i.e., narrower ovals and diamonds, with improved particle trapping characteristics when compared to the original designs. The best particle trapping performance was exhibited by the optimized geometries, which are similar to the sub-optimized designs, but with smaller post size and spacing between posts. For further details on the optimization process, the reader is referred to ref. [30].

In order to perform temperature measurements, custom-made copper-based RTDs were prepared to be integrated into the bottom part of the microdevices. The RTD microsensor device consisted of a $34.1 \mu\text{m}$ -thick copper electrode (width: 13 mm, height: 15 mm, see Fig. 2A) that was plotted from a copper clad (FR4, Single sided, 1 oz., MG Chemicals, USA) in the shape of a serpentine geometry (Fig. 2A), using a conventional printed circuit board (PCB) fabrication setup (LPKF ProtoMat S63, USA). Next, a $100 \mu\text{m}$ thick double-sided pressure-sensitive adhesive (PSA, Adhesives Research, USA) was adhered over the PCBs copper serpentine; the PSA layer was used un-pressed and was required to avoid

Table 1. Dimensions of the seven iDEP microchannel designs employed in this study

Design number	Design name	Number of rows	Number of columns	Channel width (μm)	Post size ^{a)} (μm)	Post spacing center-to-center ^{a)} (μm)
1	Original circles	4	16	1000	196.7	250
2	Original diamonds	4	16	1000	181.2	250
3	Sub-optimized ovals	4	23	880	194.4 _p and 72.0 _l	220 _p and 170 _l
4	Sub-optimized diamonds	4	23	880	193.4 _p and 112.2 _l	220 _p and 170 _l
5	Optimized ovals	12	56	1056	71.1 _p and 28.2 _l	88 _p and 68 _l
6	Optimized diamonds	12	56	1056	74.4 _p and 44.0 _l	88 _p and 68 _l
7	Channel without posts	-	-	1000	-	-

a) Sub-index **p** and **l** indicate perpendicular and longitudinal to the channel, respectively. These dimensions were measured experimentally in our lab and the standard deviations are below 4.5 μm in all cases.

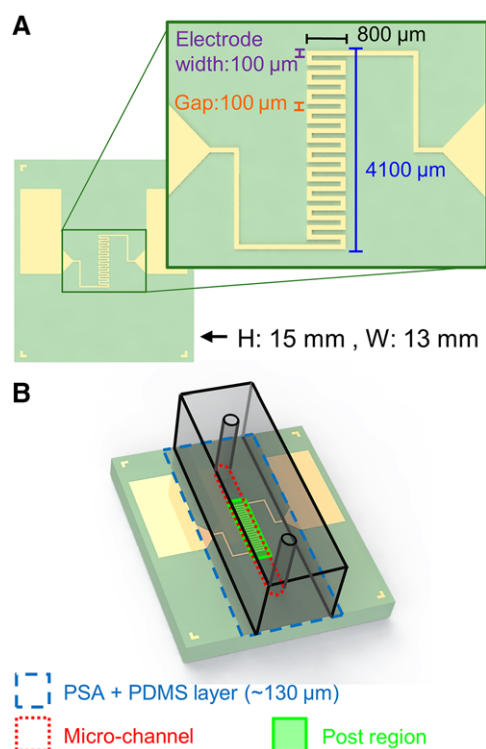


Figure 2. (A) 2D representation of the RTD sensor (top view), with a zoom in at the portion where the serpentine sensor geometry is located. (B) 3D representation of one of the devices used in this work, illustrating the PDMS microchannel bonded to the RTD sensor circuit for temperature measurement.

electrical interference between the microchannel and the sensor (detected when only a PDMS layer was used on top of the RTD copper sensor), and to ensure film flatness and reproducibility. Then, the surface was spin-coated with a PDMS mixture (as previously described) at 2500 rpm for 30 s to create a 30 μm thick polymer coating. Afterwards, the PDMS film was cured at 120°C for 10 min; the composite PSA-PDMS layer had a final thickness of 130 μm as measured using an inverted microscope (AxioVert A1, Carl Zeiss, Germany).

Finally, the microchannel and the PDMS-coated PCB were treated with air plasma for 2 min using a plasma cleaner (Harrick Plasma, Ithaca, NY, USA). Each PDMS replica was bonded by manually aligning the microchannel post region over the copper serpentine to maximize the contact area between the heated zone due to Joule heating effects and the sensor area as shown in Fig. 2B. This alignment is not critical for the study since we are measuring average temperatures and not space punctual values.

3.2 RTD sensor calibration

To calibrate the temperature response of the complete sensor system (copper serpentine + 130 μm thick PSA-PDMS composite + microchannel), a device such as the one represented in Fig. 2B was fabricated with a microchannel containing no insulating posts. In a first order approximation, the electrical resistance of a metal, such as the copper material in the serpentine, varies with temperature T according to [34, 35]:

$$R_T = R_0 [1 + \alpha (T - T_0)] \quad (5)$$

where R_T corresponds to the electrical resistance at a given T , R_0 is the electrical resistance at a reference temperature T_0 (typically 20°C), and α is the temperature coefficient of resistance for the given material (in this case, copper) [34, 35]. The calibration procedure consisted of passing deionized water at different known temperatures through the microchannel while measuring the corresponding changes in R_T (for more details on the sensor, please review the Supporting Information). To this end, four-point probe measurements were performed on the rectangular pads of the devices at a constant voltage of 1.0 mV using a source meter (Keithley 2636B, Tektronix, OR, USA) and a PCB testing circuit (see Supporting Information Fig. 1). The collected data was processed with a custom-made LabVIEW program (National Instruments, TX, USA) for real-time measurement of R_T . This procedure was used for every evaluated value of T , and, correspondingly, R_T was averaged over 1000 samples. Figure 4A illustrates the calibration curve obtained in our system.

3.3 Joule heating experiments

For these experiments, a buffer solution with conductivity of 150 $\mu\text{S}/\text{cm}$ was prepared by adding K_2HPO_4 salt crystals to deionized water until the desired conductivity was obtained. The microchannels coupled with the temperature sensor were filled with this solution as soon as they were plasma bonded to guarantee the reproducibility of the PDMS zeta potential before each experiment. Platinum wires were used as electrodes and were introduced into the inlet and outlet reservoirs of the device. A high voltage sequencer model HVS6000D (LabSmith, Livermore, CA) was used to apply DC electric potentials, which was manipulated with the software Sequence. All experiments started with a clean channel where the solution was added through the inlet reservoir until it filled the outlet. An electric potential difference of 2500 V was applied using the high voltage sequencer for 2 min and changes in the resistance of the copper material of the sensor were recorded using the same four-point probe method previously described for the calibration curve.

4 Results and discussion

4.1 Estimation of ∇E^2 as function of device geometry

The dielectrophoretic force is proportional to the gradient of the electric field square. Analyzing the spatial distribution of this gradient field allows inferring where in the microfluidic channel the dielectrophoretic force will be the strongest, or what microfluidic channel design will be the most adequate to trap a specific particle with a strong dielectrophoretic force. In Fig. 3A, the magnitude of ∇E^2 is plotted in logarithmic scale along the cutline shown in Fig. 3D. As the cutline passes exactly midway between two consecutive rows of insulating posts, where the electric field is the least uniform (see Supporting Information Fig. 3), the maximum magnitude of the gradient is captured in the plot.

A total of seven channel designs were analyzed in this work under the influence of an applied voltage of 2500 V. Six designs that contained an array of insulating posts with distinct geometries plus a channel with no insulating posts were modeled using COMSOL Multiphysics 5.3a. As expected from our previously published results [30], the optimized geometries exhibited the strongest gradient field magnitude followed by the sub-optimized and original groups of geometries. The empty microfluidic channel has the weakest gradient field magnitude in the plot as it has no insulating posts to distort the nearly uniform electric field distribution produced by the electrodes. The geometries in the optimized group exhibit a maximum gradient field magnitude higher than the original group by two and a half orders of magnitude ($\sim 10^{17.5} \text{ V}^2/\text{m}^3$ for the optimized group, $\sim 10^{15} \text{ V}^2/\text{m}^3$ for the original group).

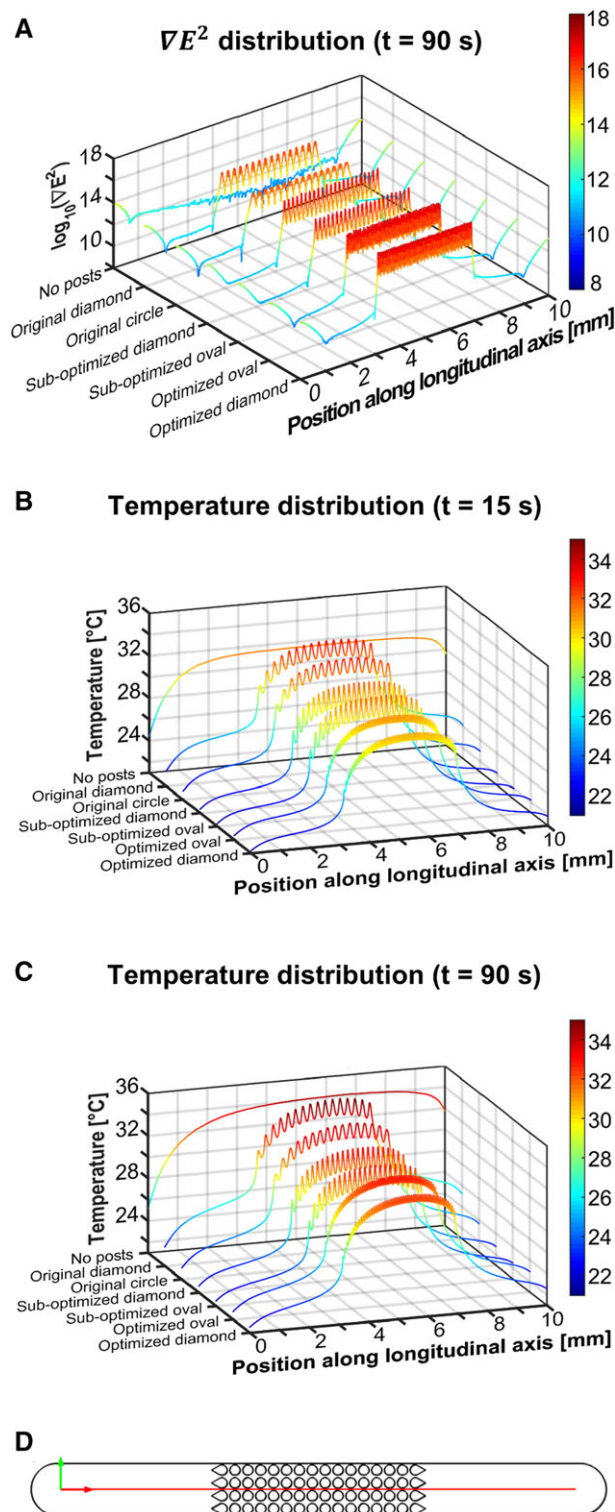


Figure 3. COMSOL simulations at a voltage of 2500 V for all six geometries studied here and a channel without insulating posts. (A) Magnitude of the $\log(\nabla E^2)$, (B) Temperature after 15 s, and (C) Temperature after 90 s. (D) Illustration of the cutline employed for evaluating the predictions in this figure.

4.2 Estimation of temperature rise as function of device geometry

It is known that electric fields generate electric currents in conductors and ionic solutions. Such currents represent heat sources in materials and devices that, as discussed earlier, can be harmful to biomaterials. Computational models of the different microfluidic channel designs allowed assessing whether the post-array optimization process influenced the temperature distribution in the fluid sample under an applied voltage of 2500 V. Figures 3B and C illustrate the temperature distribution along the cutline shown in Fig. 3D at $t = 15$ s and $t = 90$ s, respectively. The constriction regions located in the space between two adjacent rows of posts constitute “hot-spots”. These hot-spots are coincident with the location of the spots with the strongest magnitude of ∇E^2 . This behavior can be explained by analyzing the heating power (i.e., $P \sim I^2 R$) generated at hot-spots, which depends on the current going through the gap, and the resistance it offers to electrical conduction. Current passing through a gap region will depend on the combined contribution of the local current density ($\mathbf{J} = \sigma \mathbf{E}$), as well as the area available for conduction, since $I = \iint \mathbf{J} \cdot d\mathbf{A}$. Thus, heating power will be ultimately dependent on local electric field intensity and gap transversal area.

The sequence of temperature rises and falls observed in the curves exists due to the presence of electric field non-uniformities and also because of differences in thermal conductivity and heat capacity of the fluid and PDMS. Consequently, the “hot-spots” increase fluid temperature, but heat dissipation occurs immediately after leaving the area, reducing the temperature until the medium reaches the next heat source.

It can be seen from Fig. 3B that the difference in maximum temperature between the six channel designs is not significant under our experimental conditions. Original diamonds (highest temperature) heat the channel approximately 4°C more than the optimized diamond (lowest temperature). This result must be highlighted. According to the computational model, optimizing the microchannel geometry to maximize the electric field non-uniformity, and therefore, DEP trapping, has no adverse impact in terms of sample heating under the experimental conditions here tested. Examination of Fig. 3C and its comparison against Fig. 3B allows concluding that most of the heating occurs during the first seconds of the experiment, reaching a temperature plateau before one minute of electric stimulation.

Additionally, the temperature distribution of an empty channel (i.e., with no insulating posts) is shown in Fig. 3B and C as a benchmark for comparison. Interestingly, in the absence of hot-spots, most of the heating takes place close to the sample inlet. Since there are no posts inside the empty channel, there is no interfacial fluid/PDMS area at the channel center (where the posts would be) leading to no detectable rises and falls in sample temperature.

Notice that even though the optimized designs have the maximum ∇E^2 values, their temperature rise was not the

highest among all the designs. This is explained by the fact that average temperature rise will be directly related with the total generated heat power in a given design, rather than solely by the magnitude of the local electric field intensity. Generated power depends on the total electric current that passes transversally through the microfluidic device, and this current is limited by the resistance posed by the post geometry. Thus, although optimized designs will result in an increased current density at gap regions (since $\mathbf{J} = \sigma \mathbf{E}$), their reduced transversal area at the constriction site will limit the amount of passing current, increasing resistance, and thus reducing the generated heat power. Therefore, one can use electrical resistance of a microdevice design as a direct indicator of the average temperature rise (see Supporting Information Table 3 for a comparison of the different designs in terms of resistances, currents, and generated heating power, calculated from our COMSOL model). Furthermore, modifying constriction size and post geometry alters the physical system that is being heated (PDMS and water volume), as well as the fluid path and velocity. Thus, the interplay between these variables is expected to affect heat generation and convective cooling through electroosmotic flow at the same time. Although determining the interplay between the heating and cooling mechanisms is out of the scope of this work (the reader may consult [36] for a detailed discussion on this topic), our computational simulation allowed us to obtain the average temperature on the devices, which for the designs tested here differed by only $\sim 4^\circ\text{C}$.

4.3 Experimental and simulated device temperature as function of time

Figure 4A presents the behavior of the copper RTD sensor at different temperatures. The calibration curve, obtained as described earlier, shows a linear relation of the normalized resistance of the sensor with temperature. The equation of the line can be related to the dependence of the resistance of a metal to temperature, where the slope, α , is the temperature coefficient of resistance.

The equation derived from the calibration curve gives the value of the resistance R at a given temperature T (values are normalized to the resistance, R_0 , at room temperature T_0). It should be noted that the coefficient α is close to its theoretical value for copper ($0.004041\text{ }1/^\circ\text{C}$), as expected, which indicates that the sensitivity of the systems is conserved even with the $130\text{ }\mu\text{m}$ layer added between the microchannel and the sensor. This equation was used to determine temperature increases by measuring the resistance of the copper in the sensor for the dielectrophoretic experiments.

Table 2 presents a summary of the experimental results for the temperature measurements when 2500 V were applied for 2 min. It should be noticed that the maximum temperature reached in the RTD copper sensor is similar for the designs and conditions tested, i.e., between approximately 27 and 30°C . The general curve of all experiments has an initial fast heating followed by a moderate subsequent heating until

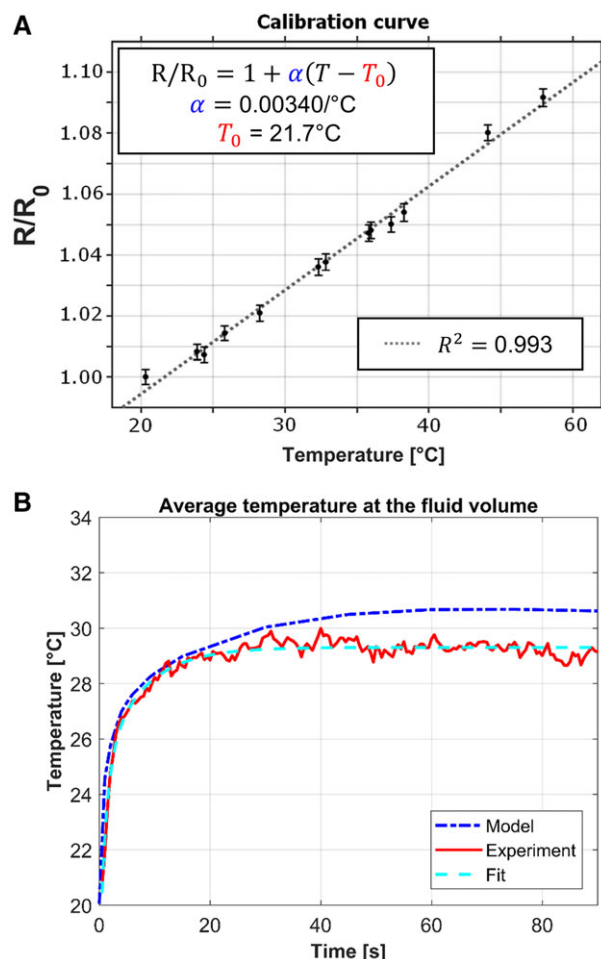


Figure 4. (A) Temperature calibration curve illustrating the normalized resistance for the RTD sensor. (B) Experimental and modeling temperature measurements for design #5, optimized oval.

reaching a steady-state around 20 s after applying the electric potential difference (Fig. 4B shows this for the channel design #5, optimized oval). This behavior is similar to the one obtained by Kale et al. [24], where temperature curves reached a plateau in around 2 min. The maximum temperature was determined experimentally by averaging the measurements given by the sensor after reaching that steady-state. The experimental temperature curves followed a double exponen-

tial behavior with R^2 greater than 0.90. The equation has the form:

$$T = T_{\infty} - Ae^{-\frac{t}{\tau_1}} - Be^{-\frac{t}{\tau_2}} \quad (6)$$

where T_{∞} is the temperature at the steady-state, A is a constant related to the first exponential with stabilization time τ_1 , and B is a constant related to the second exponential with stabilization time τ_2 [28]. A summary of the values of these constants can also be found in Table 2.

Physically, the first term of the double exponential can be associated with the heating of the liquid inside the microchannel, and the second term with the propagation of the heating to the PDMS surrounding it. While the former occurs in a short period, the latter is slower due to the lower thermal diffusivity of the material. This is reflected in greater values of τ_2 [28].

Figure 4B also illustrates the model average temperature prediction for this channel geometry. This curve was obtained through a volume average calculation for the temperature in the fluid domain. The footprint of the RTD sensor was used to define the volume for average temperature calculation. The computational prediction follows the trend established by the experimental observations. A slight deviation of less than 2°C exists for the maximum temperature, which is insignificant for most practical purposes.

4.4 Effect of suspending medium conductivity

The temperature rise in a microfluidic channel, produced by the passage of an electric current through the liquid, is not only a function of the electric field. Liquids with high electric conductivity are known to be prone to significant heating. To assess the effect of suspending medium electric conductivity on its temperature, a time-dependent parametric study was performed in COMSOL Multiphysics 5.3a. Because the six geometries with posts analyzed in this work exhibit similar heating trends under our experimental conditions, one geometry (sub-optimized oval) was selected as a representative sample for the parametric study. The computational model considered a fixed stimulation voltage of 2500 V and only the initial electrical conductivity, σ_0 , was varied, taking on the values 50, 100, 150, 200, 250, 500, and 700 $\mu\text{S}/\text{cm}$ (two below and four above the initial electrical conductivity,

Table 2. Experimental results for maximum average temperature and curve fitting following a double exponential

$$T = T_{\infty} - Ae^{-t/\tau_1} - Be^{-t/\tau_2}$$

Design name	Terminal T ($^{\circ}\text{C}$)	T_{∞} ($^{\circ}\text{C}$)	A ($^{\circ}\text{C}$)	τ_1 (s)	B ($^{\circ}\text{C}$)	τ_2 (s)	R^2
Original circles	28.13 ± 0.02	28.18	5.76	1.47	1.75	7.12	0.91
Original diamonds	26.94 ± 1.00	27.05	4.82	1.66	2.05	15.71	0.95
Sub-optimized ovals	27.30 ± 0.61	27.36	3.94	1.21	2.28	12.04	0.96
Sub-optimized diamonds	30.07 ± 0.71	30.05	5.91	1.20	3.60	6.91	0.96
Optimized ovals	29.18 ± 1.14	29.30	4.65	1.10	4.21	7.19	0.96
Optimized diamonds	27.07 ± 0.13	27.35	3.72	1.00	2.58	17.72	0.93
Channel without posts	30.96 ± 0.77	31.22	7.46	1.78	2.16	26.45	0.97

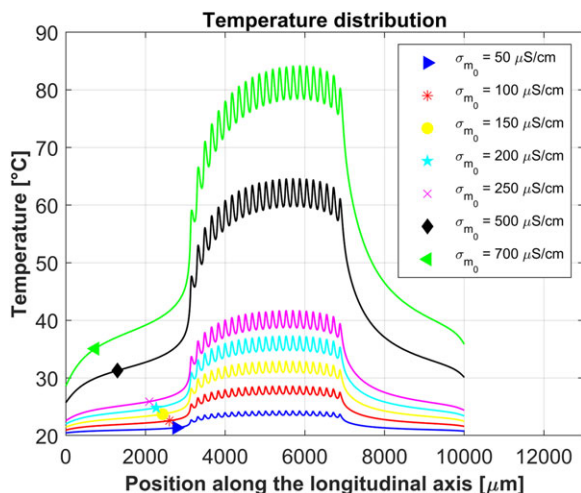


Figure 5. Prediction of the effect of suspending medium conductivity on suspending medium temperature at an applied voltage of 2500 V for 180 s, employing a sub-optimized oval geometry. Seven distinct conductivity values were modeled employing COMSOL.

$\sigma_0 = 150 \mu\text{S/cm}$, used in our experiments). The first five electric conductivity values were selected based on the reported experimental range of values for this parameter in iDEP-based devices developed for different applications [8, 37, 38]. The last two electric conductivity values were selected to produce significant heating in the microfluidic device model. The results from this study are depicted in Fig. 5. Values are taken along the same cutline illustrated in Fig. 3D for time $t = 180 \text{ s}$.

As expected, fluid temperature is proportional to electric conductivity. With an initial conductivity of $50 \mu\text{S/cm}$, a maximum instantaneous temperature of less than 25°C is predicted. Approximately 9°C below the maximum temperature predicted for the initial conductivity of $150 \mu\text{S/cm}$ used in our experiments. At the other extreme of the experimental range of values, when an initial fluid electric conductivity of $250 \mu\text{S/cm}$ is used in the simulation, the model predicts a maximum temperature of 42°C . At values of 500 and $700 \mu\text{S/cm}$ the temperature reaches values above the viability limit for bioparticles of interest (e.g., bacteria, enzymes, proteins, etc.). For the values tested in the model, a temperature rise of approximately 4.5°C is detected for each conductivity step of $50 \mu\text{S/cm}$. The temperature rise can be explained with reference to the electromagnetic heat source, Q_b , which is proportional to the current density vector $\mathbf{J} = \sigma \mathbf{E}$ (see Supporting Information Table 1). A higher conductivity translates into a larger current density that produces a stronger electromagnetic heat source. Suspending solutions with conductivities as high as $1500 \mu\text{S/cm}$ have been used to manipulate particle motion in microfluidic devices based on approaches different to that presented in this manuscript (e.g., lateral displacement) [39–41].

5 Concluding remarks

Joule heating effects in insulator-based dielectrophoretic devices were evaluated for seven distinct channel designs. The optimized devices require lower electric potential differences to effectively manipulate and trap microparticles [30], in comparison with their original and sub-optimized counterparts. When the seven designs are evaluated at the same applied voltage, temperature rises are very similar. This means that the inclusion of a higher number of posts with reduced spacing between them, which significantly enhances the distribution of ∇E^2 , has a marginal effect on the temperature increase.

These conclusions are supported by experimental and computational results presented in this work. Temperature values measured with an integrated RTD sensor are in good agreement with those simulated in a 3D COMSOL model, which considered heat dissipation in all directions from the fluid inside the channels to the PDMS walls surrounding it. It is important to highlight that the use of the RTD sensor is advantageous in comparison with the readily available Rhodamine-based temperature sensing approach. To begin with, the RTD approach presented herein does not require the addition of a temperature-sensitive molecule (i.e., Rhodamine) that can modify sample properties. Also, Rhodamine is absorbed into PDMS, significantly reducing the device's reusability and lifetime. In contrast, the RTD sensing approach is a clean method that provides similar temporal sensing accuracy.

The 3D model developed in this study can be used to determine the feasibility of using similar systems for biological applications by evaluating heating effects; while the RTD sensor can be helpful in monitoring processes where temperature is critical.

The authors would like to acknowledge the financial support provided by the National Science Foundation (Award CBET-1705895). This work was also financially supported by the Nano-Sensors and Devices Research Group of Tecnológico de Monterrey (0020209106).

The authors have declared no conflict of interest.

6 References

- [1] Hardt, S., Schönfeld, F., *Microfluidic technologies for miniaturized analysis systems*, Springer, New York 2007.
- [2] Bruus, H., *Theoretical Microfluidics*, Oxford University Press, New York 2009.
- [3] Voldman, J., *Ann. Rev. Biomed. Eng.* 2006, 8, 425–454.
- [4] Green, N. G., Ramos, A., Morgan, H., *J. Phys. D: Appl. Phys.* 2000, 33, 632–641.
- [5] Gallo-Villanueva, R., Pérez-González, V. H., Davalos, R., Lapizco-Encinas, B. H., *Electrophoresis* 2011, 32, 2456–2465.

- [6] Martínez-Duarte, R., *Electrophoresis* 2012, 33, 3110–3132.
- [7] Moncada-Hernandez, H., Baylon-Cardiel, J. L., Pérez-González, V. H., Lapizco-Encinas, B. H., *Electrophoresis* 2011, 32, 2502–2511.
- [8] Gallo-Villanueva, R. C., Rodríguez-López, C. E., Díaz-de-la-Garza, R. I., Reyes-Betanzo, C., Lapizco-Encinas, B. H., *Electrophoresis* 2009, 30, 4195–4205.
- [9] Gallo-Villanueva, R. C., Jesús-Pérez, N. M., Martínez-López, J. I., Pacheco, A., Lapizco-Encinas, B. H., *Microfluid. Nanofluid.* 2011, 10, 1305–1315.
- [10] Salmanzadeh, A., Romero, L., Shafiee, H., Gallo-Villanueva, R. C., Stremmer, M. A., Cramer, S. D., Davalos, R. V., *Lab Chip* 2012, 12, 182–189.
- [11] Rosales-Cruzaley, E., Cota-Elizondo, P. A., Sánchez, D., Lapizco-Encinas, B., *Bioproc. Biosys. Eng.* 2013, 36, 1353–1362.
- [12] Mata-Gomez, M. A., Perez-Gonzalez, V. H., Gallo-Villanueva, R. C., Gonzalez-Valdez, J., Rito-Palomares, M., Martinez-Chapa, S. O., *Biomicrofluidics* 2016, 10, 033106.
- [13] Kirby, B. J., *Micro- and Nanoscale Fluid Mechanics. Transport in Microfluidic Devices*, Cambridge University Press, New York 2010.
- [14] Lapizco-Encinas, B. H., *Electrophoresis* 2019, 40, 358–375.
- [15] Cetin, B., Li, D., *Electrophoresis* 2008, 29, 994–1005.
- [16] Gallo-Villanueva, R. C., Sano, M. B., Lapizco-Encinas, B. H., Davalos, R., *Electrophoresis* 2014, 35, 352–361.
- [17] Redmond, W. B., Bowman, B. U., *J. Bacteriol.* 1955, 69, 293.
- [18] Matsuura, Y., Takehira, M., Joti, Y., Ogasahara, K., Tanaka, T., Ono, N., Kunishima, N., Yutani, K., *Sci. Rep.* 2015, 5, 15545.
- [19] Aghilinejad, A., Aghaamoo, M., Chen, X., Xu, J., *Electrophoresis* 2018, 39, 869–877.
- [20] Chaurey, V., Rohani, A., Su, Y.-H., Liao, K.-T., Chou, C.-F., Swami, N. S., *Electrophoresis* 2013, 34, 1097–1104.
- [21] Hawkins, B. G., Kirby, B. J., *Electrophoresis* 2010, 31, 3622–3633.
- [22] Sridharan, S., Zhu, J., Hu, G., Xuan, X., *Electrophoresis* 2011, 32, 2274–2281.
- [23] Nedelcu, O. T., *Rom. J. Inf. Sci. Tech.* 2011, 14, 309–323.
- [24] Kale, A., Patel, S., Hu, G., Xuan, X., *Electrophoresis* 2013, 34, 674–683.
- [25] Prabhakaran, R. A., Zhou, Y., Patel, S., Kale, A., Song, Y., Hu, G., Xuan, X., *Electrophoresis* 2017, 38, 572–579.
- [26] Chaurey, V., Polanco, C., Chou, C.-F., Swami, N. S., *Biomicrofluidics* 2012, 6, 012806.
- [27] Gao, J., Sin, M. L., Liu, T., Gau, V., Liao, J. C., Wong, P. K., *Lab Chip* 2011, 11, 1770–1775.
- [28] Ross, D., Gaitan, M., Locascio, L. E., *Anal. Chem.* 2001, 73, 4117–4123.
- [29] Nakano, A., Luo, J., Ros, A., *Anal. Chem.* 2014, 86, 6516–6524.
- [30] Saucedo-Espinosa, M. A., Lapizco-Encinas, B. H., *J. Chromatogr. A* 2015, 1422, 325–333.
- [31] Pethig, R., Ying, H., Xiao-bo, W., Burt, J. P. H., *J. Phys. D: Appl. Phys.* 1992, 25, 881.
- [32] Marx, G. H., Huang, Y., Zhou, X. F., Pethig, R., *Microbiology* 1994, 140, 585–591.
- [33] Perez-Gonzalez, V. H., Gallo-Villanueva, R. C., Cardenas-Benitez, B., Martinez-Chapa, S. O., Lapizco-Encinas, B. H., *Anal. Chem.* 2018, 90, 4310–4315.
- [34] Dellinger, J. H., *Bulletin of the Bureau of Standards* 1911, 7, 71–101.
- [35] Fraden, J., *Handbook of Modern Sensors: Physics, Designs, and Applications*, Springer Verlag, New York 2003.
- [36] Horiuchi, K., Dutta, P., *Int. J. Heat Mass Transfer* 2004, 47, 3085–3095.
- [37] Bhattacharya, S., Chao, T.-C., Ariyasinghe, N., Ruiz, Y., Lake, D., Ros, R., Ros, A., *Anal. Bioanal. Chem.* 2014, 406, 1855–1865.
- [38] Jen, C.-P., Chen, T.-W., *Biomed. Microdev.* 2009, 11, 597–607.
- [39] Beech, J. P., Jönsson, P., Tegenfeldt, J. O., *Lab Chip* 2009, 9, 2698–2706.
- [40] McGrath, J., Jimenez, M., Bridle, H., *Lab Chip* 2014, 14, 4139–4158.
- [41] Rohani, A., Moore, J. H., Kashatus, J. A., Sesaki, H., Kashatus, D. F., Swami, N. S., *Anal. Chem.* 2017, 89, 5757–5764.